






Urban Residential Wind Field Visualization and Wind Speed Recognition System Based on Image Fusion with Health Risk Early Warning

Xin Huang¹, Lei Zhang^{2*}, Lei Huang³, Hua Zhong⁴, Yuntao Xia^{5,6}

¹ School of Architecture, Tongji Zhejiang College, Jiaxing 314001, China

² School of Architecture and Planning, Anhui Jianzhu University, Hefei 230601, China

³ Dalian Municipal Friendship Hospital, Dalian 116001, China

⁴ School of the Built Environment and Architecture, London South Bank University, London SE1 0AA, United Kingdom

⁵ Department of Information Management, Anhui Vocational College of Police Officers, Hefei 230031, China

⁶ Anhui Zhianxin Information Technology Co., Ltd., Hefei 230031, China

Corresponding Author Email: zhanglei@ahjzu.edu.cn

Copyright: ©2025 The authors. This article is published by IETA and is licensed under the CC BY 4.0 license (<http://creativecommons.org/licenses/by/4.0/>).

<https://doi.org/10.18280/ts.420239>

ABSTRACT

Received: 9 September 2024

Revised: 27 February 2025

Accepted: 13 March 2025

Available online: 30 April 2025

Keywords:

urban residential area, wind field visualization, wind speed recognition, image fusion, health risk early warning, infrared hyperspectral image, feature values of infrared hyperspectral images

With the acceleration of urbanization, improving the wind environment in urban residential areas has become a crucial issue for enhancing residents' quality of life and health safety. Traditional wind field monitoring methods have significant limitations and fail to meet the demand for large-scale, high-resolution, real-time wind field monitoring. Therefore, developing new technologies to improve the accuracy of wind field visualization and to provide scientific support for urban planning has become an urgent research need. This study proposes an urban residential wind field visualization and wind speed recognition system based on image fusion. By combining infrared hyperspectral images with their extracted feature values, a technical framework for wind field visualization and wind speed recognition is developed, leading to the implementation of a health risk early warning mechanism. Existing research primarily relies on physical models, sensor networks, and remote sensing technologies to study wind field distribution and wind speed variations; however, these methods often suffer from limitations in spatial coverage, data fusion capabilities, and computational efficiency. By introducing an innovative image fusion technique, this study overcomes the limitations of traditional approaches, offering a more precise visualization solution for urban residential wind fields. Furthermore, by leveraging feature values from infrared hyperspectral images for wind speed recognition, the system enables proactive health risk warnings. This method provides effective technical support for urban planning, environmental protection, and public health management, and holds significant theoretical and practical value.

1. INTRODUCTION

With the continuous acceleration of urbanization, the planning and design of urban residential areas are facing more and more challenges [1, 2]. The improvement of the wind environment not only affects residential comfort but also has important impacts on urban climate regulation, pollution dispersion, energy consumption, and other aspects [3-5]. The wind field distribution in urban residential areas is directly related to residents' quality of life and health safety [6, 7]. Therefore, effective monitoring and prediction of the wind field in urban residential areas are of great significance. However, traditional wind field monitoring methods mainly rely on field measurements [8], which are limited by equipment layout constraints and spatial resolution of the data [9], making it difficult to achieve real-time and accurate monitoring of large-scale urban areas. Therefore, how to improve the accuracy of wind field visualization through emerging technologies, and thus provide strong support for urban planning, has become an urgent problem to be solved.

Wind field visualization and wind speed recognition not only have important application value in architectural design, urban greening, and other fields, but also play a key role in public health and environmental management [10, 11]. Abnormal changes in wind speed may directly affect the distribution and dispersion of air pollutants [12], thereby impacting the health status of urban residents. In addition, with the intensification of global climate change and the frequent occurrence of extreme weather events [13-15], changes in the urban wind environment have also brought potential risks to residents' physical health [16, 17]. Therefore, wind field visualization and wind speed recognition based on image processing and remote sensing technology can provide scientific support for policymakers, planners, and urban managers, effectively responding to and preventing health risks caused by wind environment changes.

Existing research mainly focuses on wind field simulation based on physical models, wind speed measurement through sensor networks, and applications of remote sensing technology. However, these research methods still have some

shortcomings. Traditional wind field simulation mostly relies on limited field monitoring point data, making it difficult to fully reflect the wind speed distribution under complex urban terrains [18]. Although sensor networks can provide relatively accurate wind speed data, their deployment and maintenance costs are high, and they cannot cover large-scale areas [19]. In addition, although remote sensing images can provide some support for wind field monitoring, most methods face bottlenecks in data fusion technology and computational efficiency when processing high-resolution remote sensing images [20]. Therefore, existing research methods still need to be improved in terms of real-time performance, accuracy, and large-scale coverage capabilities of the wind field.

The main goal of this study is to propose an urban residential wind field visualization and wind speed recognition system based on image fusion technology, combining infrared hyperspectral images and the feature values of infrared hyperspectral images, to achieve precise monitoring and analysis of the urban wind field. Specifically, the research content of this paper includes two aspects: first, using infrared hyperspectral image fusion technology to realize the visualization of the urban residential wind field and accurately depict the wind speed distribution; second, through the wind speed recognition method based on the feature values of infrared hyperspectral images, accurately identify wind speed changes and predict possible health risks. This study will provide new technical means for the scientific planning and management of the urban wind environment and has important application value in fields such as health risk early warning and environmental protection.

2. VISUALIZATION OF URBAN RESIDENTIAL WIND FIELD BASED ON FUSED INFRARED HYPERSPECTRAL IMAGES

The core of the research objective in this paper is to estimate the motion vectors of atmospheric features such as water vapor or temperature changes through a global dense optical flow algorithm, and then assign appropriate heights to each motion vector. Infrared hyperspectral images can provide detailed information about different surface temperatures, humidity levels, and material properties of objects in urban areas, which are crucial for wind field studies. In the urban environment, features such as buildings, roads, and green spaces have significant impacts on the flow of wind. Infrared hyperspectral images can help analyze the variations of wind speed and temperature in different areas, thus supporting the dynamic changes of the wind field. By combining high-resolution inversion results of temperature and humidity with atmospheric motion vectors, the vertical distribution of wind can be further determined, ultimately providing accurate visualization of the wind field in urban residential areas.

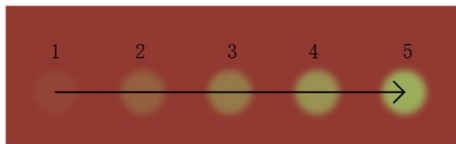


Figure 1. Schematic diagram of the dense optical flow method

The core idea of the dense optical flow method is to use changes in adjacent pixel points in the time domain of an

image sequence to calculate the optical flow field. By performing a polynomial approximation on the neighborhood information of each pixel in the image, the motion vector of each pixel is obtained, thereby constructing the motion field of the entire image. Figure 2 shows the schematic diagram of the dense optical flow method. By analyzing continuously acquired infrared hyperspectral images, the dense optical flow method can calculate the motion of each pixel in the time series. These motion vectors actually correspond to the two-dimensional plane movement of air, i.e., the wind field. To ensure the accuracy of calculation and the smoothness of visual effects, this paper adopts the image pyramid method, calculating the optical flow field layer by layer from different scales, gradually refining the details of the wind field. The main calculation process of the dense optical flow method is as follows:

2.1 Image modeling

When applying the dense optical flow method to the visualization of the urban residential wind field, image modeling must first be performed. Infrared hyperspectral images provide temperature information at each pixel, and temperature differences are often associated with changes in wind speed and wind direction. To achieve wind field visualization, it is necessary to extract temperature-related information from infrared hyperspectral images and regard the brightness changes of the image as the manifestation of airflow. In this process, image modeling not only includes the acquisition of temperature information but also involves the establishment of a time sequence of images, ensuring temporal correlation between adjacent images to reflect changes in wind speed.

Specifically, the grayscale value of the image pixel can be regarded as a function $d(a, b)$ of a two-dimensional variable. Suppose the two-dimensional column vector is represented by a , the symmetric 2×2 matrix is represented by X , the 2×1 matrix is represented by y , and the scalar is represented by z . Then, taking the pixel of interest as the center, the local image is modeled. The following equation gives the binomial expansion of the function:

$$\begin{aligned} d(a, b) &\approx e_1 + e_2 a + e_3 b + e_4 a^2 + e_5 b^2 + e_6 ab \\ &= (ab)^T \begin{pmatrix} e_4 & e_6/2 \\ e_6/2 & e_5 \end{pmatrix} \begin{pmatrix} a \\ b \end{pmatrix} + \begin{pmatrix} e_2 \\ e_3 \end{pmatrix}^T \begin{pmatrix} a \\ b \end{pmatrix} + e_1 \\ &= a^T X a + y^T a + z \end{aligned} \quad (1)$$

Assume that the neighborhood range of each pixel is $(2v+1) \times (2v+m)$, then based on the weighted least squares method, fitting the values and coordinates of the $(2v+1)^2$ pixel points in the neighborhood can obtain a six-dimensional coefficient vector for the central pixel of the image. The grayscale value matrix of the neighborhood $(2v+m) \times (2v+m)$ is split and combined into a $(2v+1)^2 \times 1$ vector d in column-major order. Let the transformation matrix Y , whose basis functions are $(1, a, b, a^2, b^2, ab)$, be composed of six column vectors y_u , with the dimension of $(2v+1)^2 \times 6$, and the coefficient vector e within the neighborhood has the dimension 6×1 . Thus:

$$d = Y \times e = \begin{pmatrix} y_1 & y_2 & y_3 & y_4 & y_5 & y_6 \end{pmatrix} \times e \quad (2)$$

When the neighborhood matrix with a two-dimensional

Gaussian distribution characteristic of size $(2v+m) \times (2v+m)$ is split and combined into a $(2v+1)^2 \times 1$ vector x in a column-priority order, the original basis function transformation matrix Y becomes:

$$d = (x \cdot y_1 \quad x \cdot y_2 \quad x \cdot y_3 \quad x \cdot y_4 \quad x \cdot y_5 \quad x \cdot y_6) \quad (3)$$

By performing dual transformation on Y , the dual transformation matrix H is obtained:

$$H = \begin{pmatrix} (x \cdot y_1, y_1) & \cdots & (x \cdot y_1, y_6) \\ \vdots & \ddots & \vdots \\ (x \cdot y_6, y_1) & \cdots & (x \cdot y_6, y_6) \end{pmatrix} \quad (4)$$

Assuming that the column vectors of the transformed basis function matrix are represented by y_u , and the cross-correlation process is represented by $*$, then at this time e is:

$$e(a) = H^{-1} \begin{pmatrix} ((x \cdot y_1) * d)(a) \\ \vdots \\ ((x \cdot y_6) * d)(a) \end{pmatrix} \quad (5)$$

2.2 Displacement estimation

Based on image modeling, the next step is displacement estimation. According to the principle of dense optical flow method, the motion of pixels between two consecutive images can be used to estimate the displacement of objects. In the application of urban residential wind field, the motion of the wind field is reflected through the pixel brightness changes caused by temperature variations in the image. By tracking the brightness value changes of each pixel, the motion vector between adjacent images can be calculated, which corresponds to the direction and magnitude of wind speed. This process is realized by solving the optical flow equation, ensuring that the motion of each pixel is consistent with that of its neighborhood pixels, satisfying the optical flow smoothness assumption. The displacement estimation process ensures that the motion of each pixel is accurately captured, thus enabling an accurate description of the wind field speed and direction within urban residential areas.

Specifically, after obtaining the coefficient vectors of pixels in two consecutive images, the optical flow field is further calculated. If a displacement d occurs between two images, it will cause changes in the expanded polynomial within the neighborhood of the image center pixel. Suppose the original position of the previous image is:

$$d_1(a) = a^T X_1 a + y_1^T a + z_1 \quad (6)$$

Assuming that the appearance information of the pixel motion scene between the two images remains unchanged, there is $X_2 = X_1$, $y_2 = (y_1 - 2X_1 f)$, $z_2 = f^T X_1 f - y_1^T f + z_1$, then after the displacement of pixels, the new position becomes:

$$\begin{aligned} d_2(a) &= d_1(a - f) \\ &= (a - f)^T X_1 (a - f) + y_1^T (a - f) + z_1 \\ &= a^T X_1 a + (y_1 - 2X_1 f)^T a + f^T X_1 f - y_1^T f + z_1 \\ &= a^T X_2 a + y_2^T a + z_2 \end{aligned} \quad (7)$$

If X_1 is a non-singular matrix, then based on $y_2 = (y_1 - 2X_1 f)$, it follows that:

$$f = -\frac{1}{2} X_1^{-1} (y_2 - y_1) \quad (8)$$

Ideally, $X_1 = X_2$, but in practical situations, this is not the case, and needs to be approximated by the average value. Let:

$$X(a) = \frac{X_1(a) + X_2(a)}{2} \quad (9)$$

$$\Delta y(a) = -\frac{1}{2} (y_2 - y_1) \quad (10)$$

Then:

$$X(a) f(a) = \Delta y(a) \quad (11)$$

$$f = (X^T X)^{-1} (X^T \Delta y) \quad (12)$$

Suppose the objective function is represented by $r(a)$, and the weight function of neighborhood pixels is represented by $q(\Delta a)$. In order to obtain the optimized displacement, let $r(a)$ represent the weight within the neighborhood of the central pixel, then the expression is:

$$r(a) = \sum_{\Delta a \in U} q(\Delta a) \|X(a + \Delta a) f - \Delta y(a + \Delta a)\|^2 \quad (13)$$

The above steps only construct the local model of the image. In order to avoid the error caused by only considering the displacement change in local polynomials at the same coordinate positions of two images, this paper introduces a priori displacement field $\tilde{f}(a)$. Assume that the pixel positions of two consecutive images are represented by a and $a + \tilde{f}(a)$, respectively, then the relative displacement estimation to the true value can be obtained by calculating the displacement difference between the two:

$$X(a) = \frac{X_1(a) + X_2(\tilde{a})}{2} \quad (14)$$

$$\Delta y(a) = -\frac{1}{2} (y_2(\tilde{a}) - y_1(a)) + X(a) \tilde{f}(a) \quad (15)$$

2.3 Scale transformation

In the visualization process of urban residential wind fields, the complexity of the wind field requires consideration of motion information at different scales. In order to effectively handle this problem, the dense optical flow method introduces the scale transformation method, usually using the image pyramid technique. The image pyramid captures wind field information at different scales through multi-level image processing. On each layer of the image, the optical flow field is first calculated, and then the high-level results are used to guide the optical flow calculation on the lower-level images. This layer-by-layer calculation method helps to handle complex influencing factors such as buildings and roads in cities, especially at low-resolution levels where large-scale

wind flow trends can be better captured, while at high-resolution levels, small-scale local wind speed variations can be finely reflected. Scale transformation ensures the step-by-step calculation process from global to local, from coarse to fine, enabling the visualization of the wind field to have both global characteristics and sufficient detail representation.

Specifically, when there are regional and global visual differences in the image, in order to accurately track the feature points in the image, this paper chooses to perform scale transformation based on the image pyramid. Suppose the scale transformation matrix is represented by $T(a)$, the following formulas give the calculation of the intermediate variables H' and g :

$$H'(a) = P(a)^T X(a)^T X(a) P(a) \quad (16)$$

$$g(a) = P(a)^T X(a)^T \Delta y(a) \quad (17)$$

Before solving the optical flow field f_{OUT} , it is necessary to perform a blurring operation on the intermediate variables H' and g . Suppose the blurred H' and g are H'_{AVG} and g_{AVG} . The optical flow field solving formula is:

$$f_{OUT}(a) = H'_{AVG}(a)^{-1} g_{AVG}(a) \quad (18)$$

3. WIND SPEED IDENTIFICATION AND HEALTH RISK EARLY WARNING BASED ON INFRARED HYPERSPECTRAL IMAGE FEATURE VALUES

The wind field in urban residential areas has complex airflow patterns, influenced by buildings, topography, and other environmental factors. These factors may cause nonlinear and local variations in wind speed. Therefore, selecting the reflectance slope of high spectral bands, the average intensity of reflected spectra, and the thermal source regions with higher radiation intensity from the infrared hyperspectral images provides effective indicators for identifying wind speed. To achieve this goal, this paper adopts the BP neural network to establish the functional relationship between feature values and the wind speed in urban residential areas. By inputting the extracted feature values from the infrared hyperspectral images, the neural network can learn the intrinsic relationship between these features and the urban wind speed and predict the wind speed based on the training data. Let the input feature values be denoted by a_u , the wind speed inversion value by O_j^{wl} , the *Sigmoid* activation function by d , and the number of nodes in the input layer, hidden layer, and output layer by l , v , and g , respectively. The neuron weights between the input layer and hidden layer and between the hidden layer and output layer are denoted by Q_{uk} and N_{kj} , and the thresholds of the hidden layer and output layer are denoted by ϕ_k and ϕ_j , respectively. The formula for a single hidden layer BP network is:

$$O_j^{wl} = d \left\{ \sum_{j=1}^g \left[n_{kj} d \left(\sum_{k=1}^v q_{uk} a_u - \phi_k \right) \right] - \phi_j \right\} \quad (19)$$

3.1 Extraction of reflectance slope feature values of hyperspectral bands

The reflectance slope reflects the response changes of

surface materials to infrared radiation of different wavelengths. The spatial influence of wind speed on the surface is manifested in the variations of the wind field; different wind speeds and directions may lead to changes in the surface reflectance of buildings, green belts, roads, etc. When the wind speed is high, the thermal source regions and reflected spectra on the surface undergo varying degrees of change, affecting the reflectance slope of the hyperspectral image. By analyzing these slope changes, the characteristics of the wind field under different wind speeds can be identified, thereby providing a reliable basis for wind speed estimation.

To ensure the accuracy of the extracted reflectance slope, the first step is to remove the baseline noise, thereby eliminating signal deviations caused by environmental interference, sensor noise, and other factors. Baseline noise may cause inaccuracies in the reflectance data of hyperspectral images, which would further affect the accuracy of subsequent wind speed identification. In the environment of urban residential areas, the infrared band reflection characteristics of different types of surface features, such as buildings, roads, and green spaces, may generate errors due to the presence of such noise. This paper selects the region before the "flicker zone" without scattering signals in the infrared hyperspectral image as the baseline noise calculation region. Assuming the baseline noise at a certain moment is represented by σ_{NO} , and the number of pixels in the baseline noise calculation region is denoted by V , the specific calculation formula is:

$$\sigma_{NO} = \frac{1}{V} \sum_{\pi=-1.0}^{-2.25} \sum_{f_d=-2.5}^{2.0} B(\pi, d_f) \quad (20)$$

After subtracting the baseline noise, the scattered signal power value $B(\pi, d_f)$ can be calculated by the following formula:

$$\bar{B}(\pi, d_f) = B(\pi, d_f) - \sigma_{NO} \quad (21)$$

The second step is the generation of the delayed integration waveform. The generation of the delayed integration waveform is achieved by integrating the radiation intensity at different bands of the hyperspectral image over time or space. The wind speed in urban residential areas is usually influenced by factors such as building clusters, green spaces, and road network layouts; therefore, changes in the wind field will affect the intensity and distribution of surface thermal radiation. By generating the delayed integration waveform, a comprehensive reflection intensity waveform can be obtained, which can reflect the changes in the reflectance of building surfaces, roads, and green areas under different wind speeds. In this paper, incoherent integration is performed over the selected range of the infrared hyperspectral image, assuming the Doppler frequency shift range of the window is denoted by Δd_f . When the Doppler frequency shift range is Δd_f , the function of delay-scattering power is represented by $F(\pi_k, \Delta d_f)$. The number of Doppler points corresponding to each fixed delay in the image is denoted by L , and the calculation formula is:

$$F(\pi_k, \Delta d_f) = \frac{1}{L} \sum_{l=1}^L \bar{B}(\pi_k, d_{f_l}) \quad (22)$$

After denoising and generating the delayed integration waveform, the reflectance slope of the hyperspectral band is

calculated. In urban residential areas, the changes in wind speed directly affect the surface temperature distribution and radiation intensity, thereby influencing the changes in reflectance. The reflectance slope is a measure of the rate of change of reflectance with respect to wavelength, which can reveal the changes in surface reflectance characteristics caused by wind speed in different regions. In areas with higher wind speeds, the reflectance changes more sharply. Therefore, by calculating the reflectance slope of the hyperspectral bands, the extent to which wind speed affects the surface material reflectance characteristics can be determined. Specifically, the leading edge region centered around the leading center point of the delayed integration waveform is fitted with a first-order polynomial to obtain the slope of the best fit line. Assuming the delay and Doppler frequency shift ranges for calculating the reflectance slope of the hyperspectral band are $\Delta\pi$ and Δd_f , and the slope and intercept of the best fit line are denoted by x and z , the calculation formula is:

$$\beta_{LES}(\Delta\pi, \Delta d_f) = \underset{\beta, z}{\text{ARGMIN}} \left\{ \left[\sum_{k=1}^2 F(\pi_k, \Delta d_f) - (\beta\pi_k + z) \right]^2 \right\} \quad (23)$$

3.2 Extraction of average intensity characteristic value of reflectance spectrum

The average intensity of the reflectance spectrum refers to the overall response intensity of the surface to infrared radiation, which contains important meteorological information. Buildings and other surface features in urban residential areas are affected by solar radiation during the daytime, while at night, they exhibit different thermal radiation characteristics. Wind speed has an indirect impact on the average intensity of the reflectance spectrum, especially under conditions of high wind speed, where changes in the wind field cause uneven distribution of heat sources in the air, thereby affecting the radiation intensity of the surface. By comparing the average intensity of the reflectance spectrum in different regions, the distribution of wind speed can be determined, thus identifying the characteristics of the wind field. This characteristic value provides a quantitative basis for thermal source distribution changes in wind speed identification.

$$\alpha_{FLX}(\Delta\pi, \Delta d_f) = \frac{\sum_k^V \sum_l^L \bar{B}(\pi_k, d_{f_l})}{LV} \quad (24)$$

3.3 Extraction of characteristic value of high radiation intensity thermal source area

High radiation intensity thermal source areas usually represent local thermal concentration regions, which are often closely related to wind speed changes. Buildings, roads, and green spaces in urban residential areas exhibit different variation patterns of thermal radiation intensity under different wind speeds. Stronger wind speeds may intensify the radiation intensity differences of thermal source areas, affecting the distribution of thermal sources in hyperspectral images. Therefore, the analysis of high radiation intensity areas can effectively reflect the impact of wind speed on surface thermal distribution, thus providing strong support for wind speed

identification. These characteristic values help extract key indicators of wind speed changes from infrared hyperspectral images, aiding in precise wind speed monitoring and health risk warning in urban environments.

$$\delta_{YEZT} = (4\pi)^3 \frac{B_{\pi, df} U_{\pi, df} M_{s2t} M_{s2e} E_S^2 E_E^2}{\eta^2 O^S H_{io}^S H_{io}^E} \quad (25)$$

Assuming that the scattering signal power of the high radiation intensity thermal source areas in the image is represented by $B_{\pi, df}$, the loss correction introduced by the average intensity of the reflectance spectrum is represented by $U_{\pi, df}$, and atmospheric loss corrections are represented by M_{s2t} and M_{s2e} . The wavelength is represented by η , the signal transmission power in the reflection direction of high radiation intensity thermal source areas is represented by O^S , the reflection signal gains of high radiation intensity thermal source areas are represented by H_{io}^S and H_{io}^E , and the distances from the image shooting point to the ground are represented by E^S and E^E .

3.4 Multi-feature-value-based wind speed identification method

Since the characteristic values extracted from infrared hyperspectral images have significant numerical differences, in order to prevent the characteristic values with lower numerical values from being overwhelmed in subsequent analysis, and to accelerate the learning and convergence speed of the BP neural network, this paper adopts a normalization processing method. Normalization maps each characteristic value into the [0,1] interval, ensuring that all characteristic values are within the same numerical range, thus improving the stability of the data and the learning efficiency of the neural network. Especially in the urban residential wind field, the variation of wind speed in different regions affects the characteristic values such as reflectance and radiation intensity in infrared hyperspectral images differently. Through preprocessing, the magnitude differences among these characteristic values are reduced, thereby enabling better inversion and identification of wind speed. Assuming that the characteristic value is represented by a , the normalized characteristic value is represented by a' , and the maximum and minimum values in the characteristic value dataset are represented by a_{MAX} and a_{MIN} respectively, the specific formula is:

$$a' = \frac{a - a_{MIN}}{a_{MAX} - a_{MIN}} \quad (26)$$

Furthermore, based on different combinations of characteristic values, this paper establishes a wind speed inversion model using a BP neural network. Wind speed inversion does not rely solely on a single characteristic value but forms a more comprehensive feature matrix by combining multiple characteristic values. To verify the inversion performance under different feature value combination methods, two-dimensional or three-dimensional feature matrices were selected as inputs to the BP neural network, and multiple tests were conducted to optimize the network structure. Considering the balance between network learning efficiency and effectiveness, this paper set the number of hidden layer nodes to 5 and 6 respectively, and used training

and validation sets for model training. The BP neural network learns the wind speed variation patterns in the multidimensional feature matrix, enabling more accurate identification of wind speed in the urban residential wind field. This multi-feature-value combination method not only improves the accuracy of wind speed identification but also provides more reliable wind speed data support for health risk warnings.

Further specific strategies for health risk warnings need to combine the correlation between wind speed and air quality, building structure, and environmental factors within urban residential areas. By analyzing the air flow patterns under different wind speed conditions, areas where excessively high wind speed may cause the accumulation or dispersion of air pollutants, such as PM2.5, nitrogen dioxide, and other harmful gases, can be identified. Combined with existing health risk data, real-time air quality warnings can be provided to residents in these areas. When monitoring detects excessively high wind speeds that may cause an increase in pollutant concentrations, the system will automatically trigger warnings to remind residents to take corresponding health protection measures, such as wearing masks, reducing outdoor activities, or closing windows. These correlations between wind speed and pollutant concentrations will be monitored and predicted in real-time through big data analysis models to timely identify potential health risks.

4. EXPERIMENTAL RESULTS AND ANALYSIS

Figure 2 shows multiple types of residential areas in Jiaxing, covering high-, medium-, and low-density determinant slab

residential areas, including Sujia Zhijingyuan, Vanke Guangnianli Future Community, Huoju Community (Xincheng Town), Xingfuli Future Community, Hongxiang Tianyufu Future Community, Nanjiang Apartment, Mengdie Huayuan, Shuangxi Garden, Jindi Minglu Mansion, Jiaxing Lake Shore Pearl Home, Yanjing Community, and New Hope Jinlin Minglu, etc. These residential areas are distributed in different regions of Jiaxing, with differences in building layout, floor area ratio, and other aspects, providing rich and diverse research samples for the experimental study of the image-fusion-based urban residential wind field visualization, wind speed identification system, and health risk early warning.

The determinant slab residential area cases of different densities, with their building arrangement, spacing between buildings, and surrounding environments, significantly affect wind field characteristics. High-density residential areas have relatively compact buildings, which may lead to complex local wind speed changes and obvious airflow interference; medium- and low-density residential areas have larger spacing between buildings, and the wind field is relatively open, but may also be affected by surrounding topography, road orientation, and other factors. Through wind field visualization and wind speed identification of these typical case samples, the characteristics of wind environments in different residential areas can be deeply studied, providing basic data for health risk early warning. It also helps assess the potential impact of the wind environment on residents' health, such as the accumulation of air pollutants caused by poor ventilation, the intensification of the heat island effect, etc., thus providing scientific basis for optimizing urban residential planning and design.



Figure 2. Typical case samples of wind field visualization for high-, medium-, and low-density determinant slab residential areas in Jiaxing

Figure 3 shows multiple height layouts and residential building type models used in the experiments, presented in the form of three-dimensional columnar diagrams. Different columns represent different residential buildings, with differences in height and arrangement mode among the models. Observing from left to right and top to bottom, the models

cover a variety of combinations of building heights and arrangement patterns, reflecting diversified residential building types and layouts, providing rich material for studying wind field characteristics under different spatial forms.

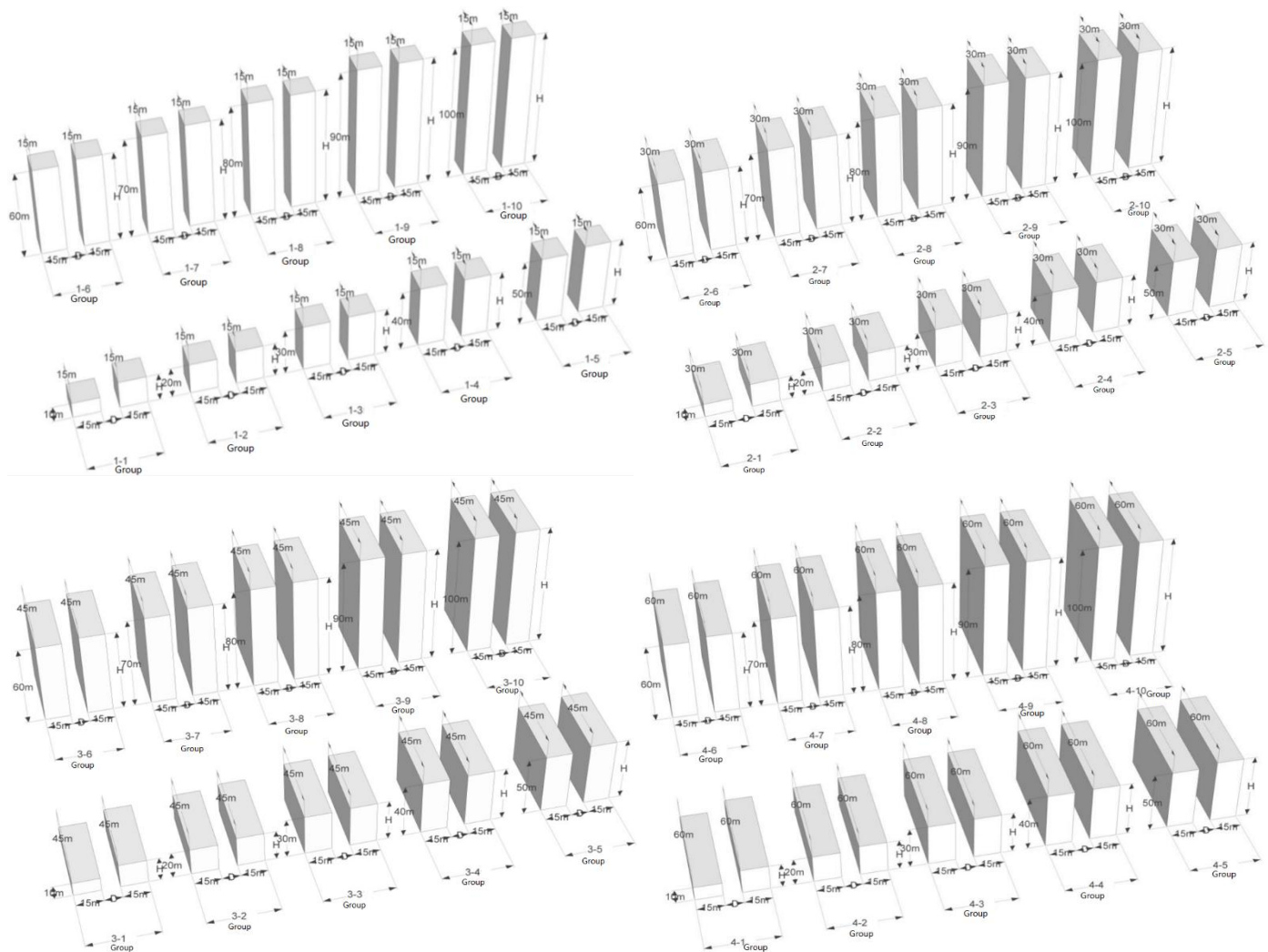


Figure 3. Height layouts and residential building type models used for the experiment

From Figure 4, it can be seen that in both the training set and test set, there are differences in the inversion accuracy of the wind field U and V components under different weight settings and feature combination values. For the wind field U component, under different pressure values, the root mean square error (RMSE) values of the wind field U component with various weight combinations show different change trends. In the test set, when the weight is set as 0.2, 0.4, and 0.4 for the three feature combination values (black solid line), within a certain pressure range, the RMSE value of the wind field U component is relatively low. For the wind field V component, similarly in both the training set and test set, the RMSE values vary with different weight combinations. When the weight is set as 0.2, 0.4, and 0.4 for the three feature combination values (black solid line), in some pressure intervals, the RMSE value is lower than other weight combinations, showing better inversion accuracy. Overall, the weight setting of 0.2, 0.4, and 0.4 for the three feature combination values has a clear advantage in the inversion of wind field U and V components.

Figure 5 shows the variation of the simulated brightness temperature of the wind field with wavenumber under the pressure conditions of 200hPa and 500hPa. Under 200hPa pressure, the simulated brightness temperature data is marked with red asterisks. In the wavenumber range of 1600 - 2300 cm^{-1} , the simulated brightness temperature shows a certain fluctuation trend, with the value range roughly between 230 -

300K. Under 500hPa pressure, the simulated brightness temperature data is marked with blue triangles. Similarly, within the wavenumber range of 1600 - 2300 cm^{-1} , the simulated brightness temperature also fluctuates, with the value range roughly between 220 - 300K. Under the two pressure conditions, the fluctuation trend and range of the simulated brightness temperature with wavenumber are different. From the data, it can be seen that different pressures cause differences in the variation of the simulated brightness temperature of the wind field with wavenumber. This indicates that pressure is an important factor affecting the relationship between simulated brightness temperature and wavenumber in the wind field, which is of great significance for using infrared hyperspectral images for urban wind field monitoring and analysis.

Figure 6 shows the displacement distribution identified under different frame numbers at the pressure conditions of 200hPa and 500hPa. Under 200hPa pressure, the horizontal axis represents frame numbers (1 - 100), and the vertical axis represents displacement (m). Different colored points represent different displacement values, with the displacement value range roughly between 0 - 2m. The displacement distribution corresponding to each frame number is relatively scattered, with no obvious concentration trend. Under 500hPa pressure, similarly with frame numbers as the horizontal axis and displacement as the vertical axis, the displacement value range is also between 0 - 2m. The displacement distribution

across different frame numbers is also relatively scattered and differs from the distribution under 200hPa pressure. From the data, it can be seen that under the conditions of different pressures (200hPa and 500hPa), as the frame number changes, the identified displacement distribution shows different

characteristics. This indicates that pressure has a significant impact on displacement distribution identified based on infrared hyperspectral images, and the displacement distribution is closely related to wind speed, thereby affecting wind field monitoring and analysis.

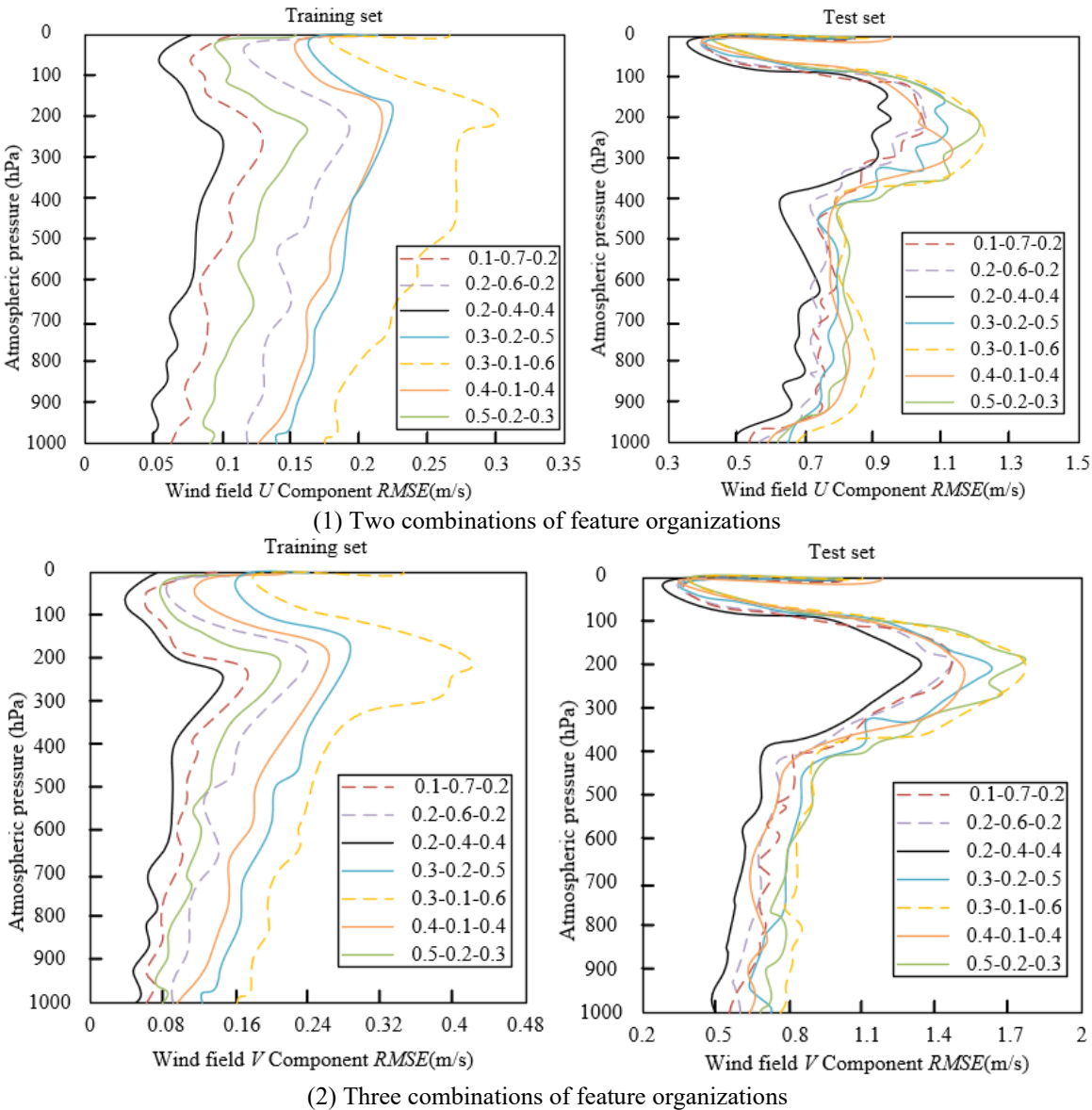


Figure 4. Comparison of wind field U and V component inversion accuracy under different weight settings and feature combination values

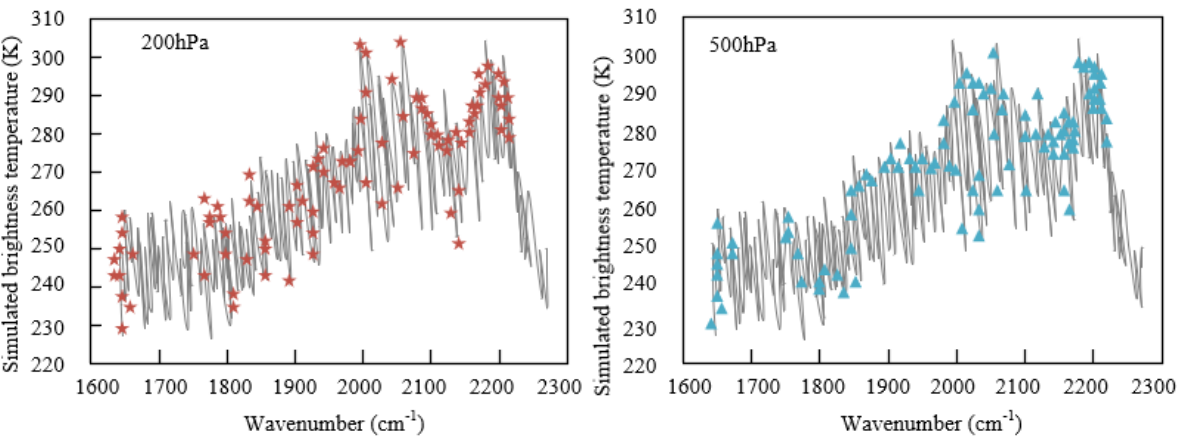


Figure 5. Influence of wavenumber on simulated brightness temperature of wind field at 200hPa and 500hPa

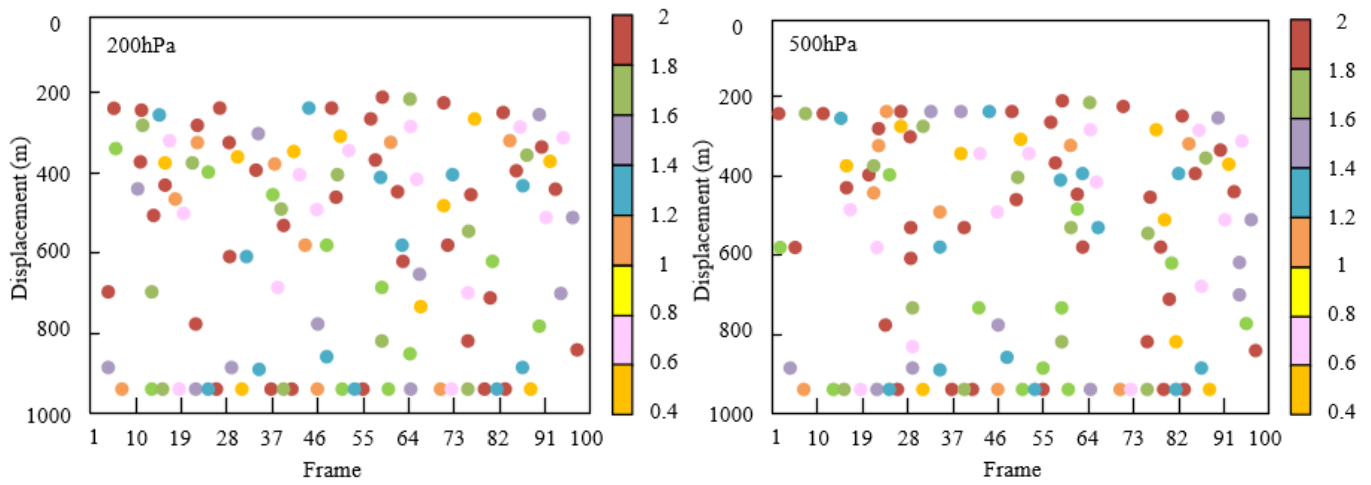


Figure 6. Displacement distribution identified under different frame numbers

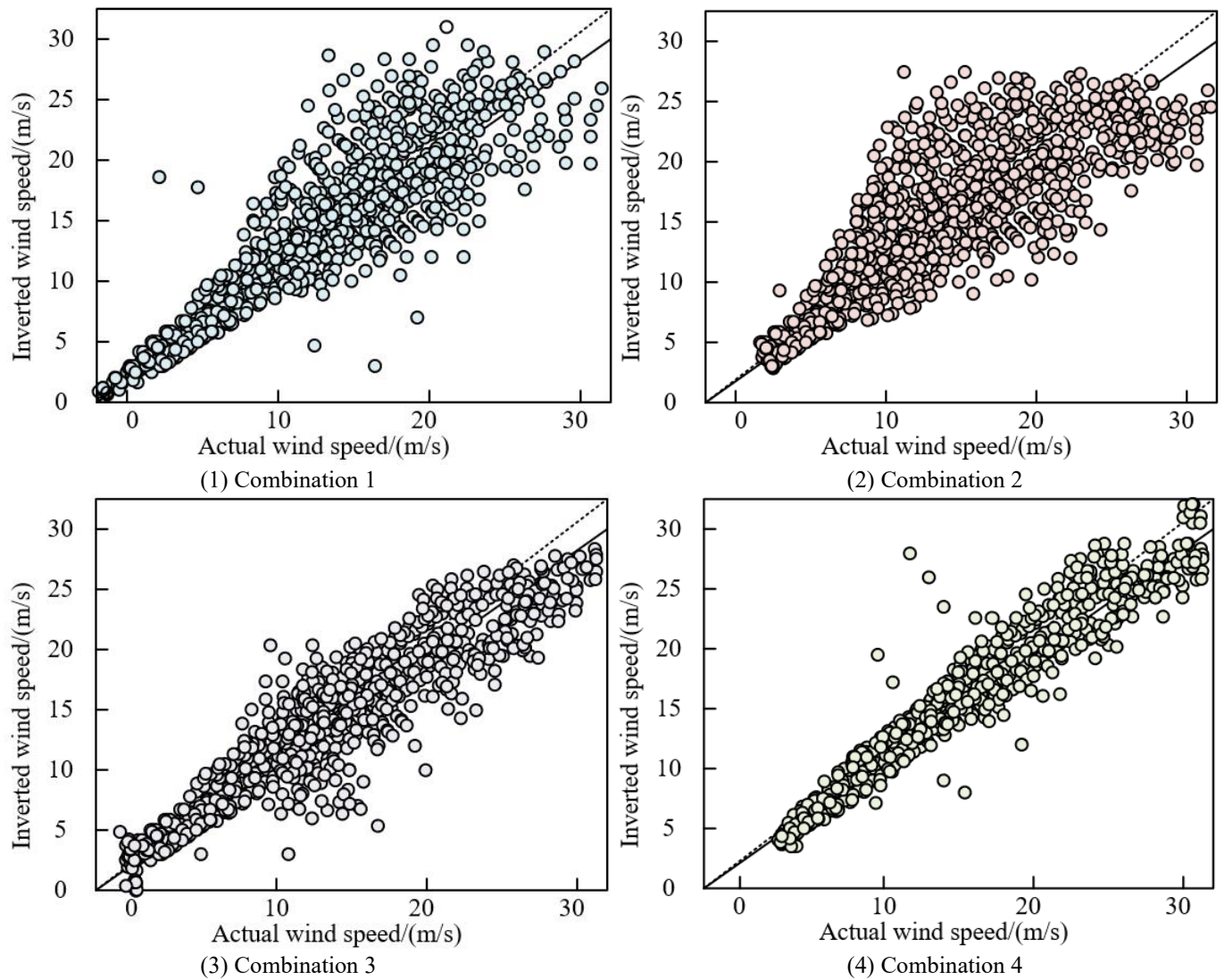


Figure 7. Comparison between wind field inversion values and real values under different feature combination conditions

Table 1. Fitting results of infrared hyperspectral image feature values under different combinations

	Combination 1	Combination 2	Combination 3	Combination 4
Pearson correlation coefficient	0.936	0.874	0.915	0.948
Root Mean Square Error (RMSE)	2.14	3.21	2.26	1.78
Mean Relative Error (MRE)	2.68	7.89	5.89	2.56

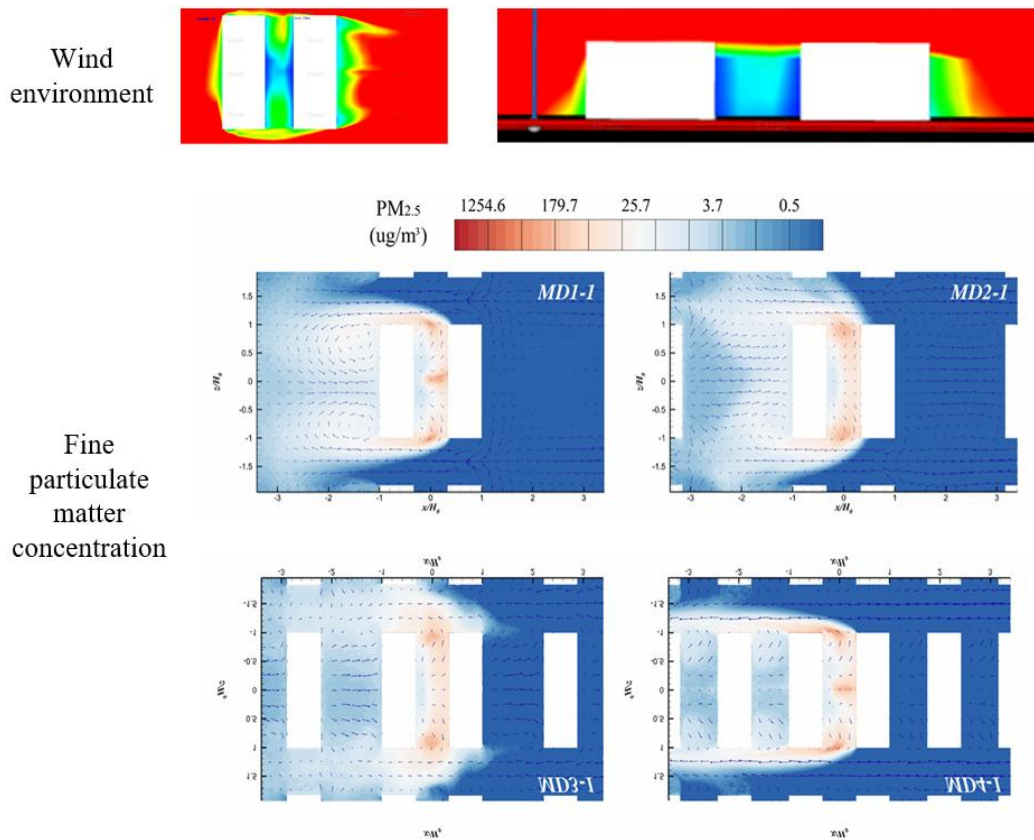


Figure 8. Example of wind environment and fine particulate matter concentration and flow field distribution simulation experiment in the equal-height model

Figure 7 shows the comparison between wind field inversion values and real values under different feature combination conditions. In the figure, combinations 1 to 4 correspond respectively to: the reflectance slope of hyperspectral bands + the average intensity of the reflected spectrum; the reflectance slope of hyperspectral bands + thermal source areas with higher radiation intensity; the average intensity of the reflected spectrum + thermal source areas with higher radiation intensity; and the combination of all three features in four situations. The four subfigures correspond respectively to combinations 1 to 4, where the horizontal axis is the actual wind speed and the vertical axis is the inverted wind speed. In combination 1, the data points are relatively scattered, with some points deviating from the diagonal line, indicating that there is a certain deviation between the inverted wind speed and the actual wind speed; in combination 2, the data points are also unevenly distributed, with relatively obvious deviations in high wind speed areas; in combination 3, the data points are relatively concentrated near the diagonal line, but there are still some scattered points; in combination 4, the data points are most concentrated around the diagonal line, indicating a relatively high degree of fit between the inverted wind speed and the actual wind speed. Overall, different feature combinations have a significant impact on wind field inversion accuracy. Combination 4 performs the best in wind field inversion, with the inverted wind speed being closer to the actual wind speed, thus more accurately reflecting the real wind speed situation.

According to the data shown in Table 1, the experimental results reveal the performance of infrared hyperspectral image feature value fitting under different combinations. Specifically, combination 1 and combination 4 show relatively high Pearson correlation coefficients, at 0.936 and 0.948

respectively, indicating that these two combinations can more accurately capture the linear relationship between wind speed and infrared hyperspectral image features. In addition, the RMSE of combination 1 and combination 4 are 2.14 and 1.78 respectively; the lower RMSE indicates that these combinations have smaller prediction errors in the fitting process. In terms of MRE, combination 1 and combination 4 also perform well, at 2.68 and 2.56 respectively, further proving their effectiveness in accurately predicting wind speed and health risks. In contrast, combination 2 and combination 3 perform worse in terms of Pearson correlation coefficient, RMSE, and MRE, especially combination 2, whose MRE is as high as 7.89, showing greater uncertainty during the fitting process. Through the analysis of experimental results, it can be concluded that the feature combinations of combination 1 and combination 4 perform better in wind speed recognition and health risk warning applications. This is because they can more effectively capture the correlation between wind speed changes and relevant thermal source areas through the selection of hyperspectral image features, especially in complex environments of urban residential areas, enabling more accurate identification and prediction of wind speed changes. Moreover, the lower RMSE and MRE of combination 1 and combination 4 indicate their higher stability in practical applications, making them suitable for real-time wind speed monitoring and health risk warning. On the contrary, the relatively high errors and low correlation coefficients of combination 2 and combination 3 suggest that they are less applicable to the current wind speed recognition tasks and thus require further optimization of feature selection and fusion methods.

Figure 8 shows an example of the simulation experiment of the wind environment and fine particulate matter

concentration and flow field distribution in the equal-height model. The wind environment part visualizes wind field characteristics through color, while the fine particulate matter concentration part combines flow field arrows and concentration color scales to show distribution. In models such as MD1-1 and MD2-1, the flow field arrows show the flow direction of the wind, and the concentration distribution is reflected by the depth of color; areas with high concentrations are closely related to the flow field morphology, reflecting the accumulation and diffusion characteristics of fine particulate matter under different wind field conditions. This simulation experiment verified the effectiveness of the wind environment and pollutant diffusion model in the health risk warning system. Wind field characteristics directly affect the diffusion paths and concentration distribution of fine particulate matter. In areas with larger wind speeds or smooth flow fields, the concentration of fine particulate matter is lower, indicating that the wind promotes pollutant diffusion; in areas with smaller wind speeds or complex flow fields, fine particulate matter easily accumulates, and the concentration is higher. This shows that through wind field visualization and wind speed recognition, pollutant distribution can be accurately predicted, providing reliable evidence for health risk warning, and proving the practicality and scientific value of the model in revealing the relationship between wind environment and pollutant diffusion and assisting health risk assessment.

5. CONCLUSION

This study proposed a city residential area wind field visualization and wind speed recognition system based on image fusion technology, aiming to provide technical support for accurate monitoring of urban wind fields and health risk warning by combining infrared hyperspectral images and image feature values. First, the study successfully realized the visualization of wind fields in urban residential areas by using infrared hyperspectral image fusion technology, accurately depicting the wind speed distribution under different wind speed conditions. This process, through the extraction and fusion of multidimensional feature data from hyperspectral images, can comprehensively and intuitively display the spatial distribution of wind speed changes. In addition, the study proposed an efficient wind speed recognition method combined with infrared hyperspectral image feature values, which can not only accurately recognize wind speed changes but also further predict health risks caused by wind speed changes. The experimental results show that through image fusion technology and feature value combinations, the accuracy of wind speed recognition has been significantly improved, providing a feasible technical path for health risk prediction in urban environments.

Through the wind speed recognition system in the main text, it helps in wind environment control during residential area planning and form design, can reduce the diffusion of atmospheric pollutants, intervene in health risks such as respiratory diseases and heat stress among residents, and shows its potential in public health warning, assisting healthy city and residential area construction. Establishing the linkage mechanism among city residential wind field visualization - wind speed recognition system - health risk warning can provide accurate technical support for healthy community and healthy city planning and design, offering practical decision-making tools for urban planners. Jiaxing belongs to the hot

summer and cold winter area, and currently, the urban residential areas are mainly medium-density residential areas. The analysis of wind field visualization and wind speed recognition system and its health risk warning potential based on image fusion will provide a scientific basis for wind environment optimization in urban residential areas, assisting Jiaxing in developing towards "low-density high-quality, medium-density with good supporting facilities, high-density with strong vitality" healthy communities.

However, although this study has achieved good results in wind speed recognition and health risk warning, there are still certain limitations. First, the study relies on the quality and resolution of hyperspectral images, and the acquisition of these images may be affected by equipment, environment, and shooting conditions, thus affecting the accuracy of wind speed recognition. Secondly, the current models and methods are mainly targeted at some typical urban residential areas and lack adaptability to wider urban environments or extreme weather conditions. Therefore, future research can focus on how to further optimize image fusion algorithms and feature extraction methods to improve adaptability and robustness under different urban areas and weather conditions. In addition, integrating more sensor data for multi-source information fusion can improve the accuracy and real-time performance of wind speed recognition and health risk warning. Future research should also consider how to achieve real-time deployment of the system and establish an intelligent urban wind field monitoring and health risk warning platform to help improve the quality of life of urban residents and reduce the negative impact of wind speed changes on health.

FUNDING

This paper was supported by Public Welfare Research Program of Jiaxing Municipal Science and Technology Plan Project (Grant No.: 2025CGZ077); National Key Research and Development Program (Grant No.: 2022YFC380020); 2025 General Research Project of Zhejiang Provincial Education Science Planning (Grant No.: 2025SCG165); the Second Batch of Teaching Reform Projects implemented by Ordinary Undergraduate Universities in Zhejiang Province under the '14th Five-Year Plan' Framework (Grant No.: JGBA2024724).

REFERENCES

- [1] Ilyichev, V.A., Kolchunov, V.I., Bakaeva, N.V., Kormina, A.A. (2021). Urban environment design: new methodological approaches based on the biosphere compatibility paradigm (part 2). *Russian Journal of Building Construction and Architecture*, 4: 115-130. <https://doi.org/10.36622/VSTU.2021.52.4.011>
- [2] Theis, J., Woolley, C.K., Seddon, P.J., Shanahan, D.F., Freeman, C., Pedersen Zari, M., van Heezik, Y. (2025). The New Zealand biodiversity factor—Residential (NZBF-R): A tool to rapidly score the relative biodiversity value of urban residential developments. *Land*, 14(3): 526. <https://doi.org/10.3390/land14030526>
- [3] Ramarajan, J., Jayavel, S. (2023). Effect of in-phase type waviness in the walls of a confined Savonius rotor placed in a long channel. *Journal of Mechanical Science and Technology*, 37(5): 2395-2403.

- <https://doi.org/10.1007/s12206-023-0416-7>
- [4] Tominaga, Y., Mochida, A., Yoshie, R., Kataoka, H., Nozu, T., Yoshikawa, M., Shirasawa, T. (2008). AIJ guidelines for practical applications of CFD to pedestrian wind environment around buildings. *Journal of Wind Engineering and Industrial Aerodynamics*, 96(10-11): 1749-1761. <https://doi.org/10.1016/j.jweia.2008.02.058>
 - [5] Wang, B., Cot, L.D., Adolphe, L., Geoffroy, S., Sun, S. (2017). Cross indicator analysis between wind energy potential and urban morphology. *Renewable Energy*, 113: 989-1006. <https://doi.org/10.1016/j.renene.2017.06.057>
 - [6] Kubota, T., Miura, M., Tominaga, Y., Mochida, A. (2008). Wind tunnel tests on the relationship between building density and pedestrian-level wind velocity: Development of guidelines for realizing acceptable wind environment in residential neighborhoods. *Building and Environment*, 43(10): 1699-1708. <https://doi.org/10.1016/j.buildenv.2007.10.015>
 - [7] Shin, Y., Park, S., Yun, H., Yu, M. (2022). Urban wind field mapping technique for municipal environmental planning: A case study of Cheongju-Si, Korea. *Atmosphere*, 13(11): 1805. <https://doi.org/10.3390/atmos13111805>
 - [8] Park, J.Y., Lee, J.K., Oh, K.Y., Lee, J.S. (2014). Development of a novel power curve monitoring method for wind turbines and its field tests. *IEEE Transactions on Energy Conversion*, 29(1): 119-128. <https://doi.org/10.1109/TEC.2013.2294893>
 - [9] Asmine, M., Langlois, C.É. (2016). Field measurements for the assessment of inertial response for wind power plants based on Hydro-Québec TransÉnergie requirements. *IET Renewable Power Generation*, 10(1): 25-32. <https://doi.org/10.1049/iet-rpg.2015.0143>
 - [10] Shafii, S., Obermaier, H., Linn, R., Koo, E., Hlawitschka, M., Garth, C., Joy, K.I. (2013). Visualization and analysis of vortex-turbine intersections in wind farms. *IEEE Transactions on Visualization and Computer Graphics*, 19(9): 1579-1591. <https://doi.org/10.1109/TVCG.2013.18>
 - [11] Cao, Y., Mo, Z., Ai, Z., Wang, H., Xiao, L. (2016). An efficient and visually accurate multi-field visualization framework for high-resolution climate data. *Journal of Visualization*, 19: 447-460. <https://doi.org/10.1007/s12650-015-0335-5>
 - [12] Weerasinghe, R.M., Pannila, A.S., Jayananda, M.K., Sonnadara, D.U.J. (2016). Multifractal behavior of wind speed and wind direction. *Fractals*, 24(1): 1650003. <https://doi.org/10.1142/S0218348X16500031>
 - [13] Sippel, S., Meinshausen, N., Fischer, E.M., Székely, E., Knutti, R. (2020). Climate change now detectable from any single day of weather at global scale. *Nature Climate Change*, 10(1): 35-41. <https://doi.org/10.1038/s41558-019-0666-7>
 - [14] Gable, L. (2023). Global health law and the climate crisis: An unfulfilled opportunity. *Journal of Law, Medicine & Ethics*, 51(3): 694-697. <https://doi.org/10.1017/jme.2023.124>
 - [15] Nassanga, G. (2020). Translating the global climate change challenge into action as reflected in Uganda's media. *Journal of African Media Studies*, 12(3): 267-281. https://doi.org/10.1386/jams_00024_1
 - [16] Ku, C.A., Tsai, H.K. (2020). Evaluating the influence of urban morphology on urban wind environment based on computational fluid dynamics simulation. *ISPRS International Journal of Geo-Information*, 9(6): 399. <https://doi.org/10.3390/ijgi9060399>
 - [17] Ishugah, T.F., Li, Y., Wang, R.Z., Kiplagat, J.K. (2014). Advances in wind energy resource exploitation in urban environment: A review. *Renewable and Sustainable Energy Reviews*, 37: 613-626. <https://doi.org/10.1016/j.rser.2014.05.053>
 - [18] Ren, H., Laima, S., Chen, W. L., Zhang, B., Guo, A., Li, H. (2018). Numerical simulation and prediction of spatial wind field under complex terrain. *Journal of Wind Engineering and Industrial Aerodynamics*, 180: 49-65. <https://doi.org/10.1016/j.jweia.2018.07.012>
 - [19] Rehman, S. (2014). Tower distortion and scatter factors of co-located wind speed sensors and turbulence intensity behavior. *Renewable and Sustainable Energy Reviews*, 34: 20-29. <https://doi.org/10.1016/j.rser.2014.03.007>
 - [20] Amarin, R.A., Jones, W.L., El-Nimri, S.F., Johnson, J.W., Ruf, C.S., Miller, T.L., Uhlhorn, E. (2011). Hurricane wind speed measurements in rainy conditions using the airborne Hurricane Imaging Radiometer (HIRAD). *IEEE Transactions on Geoscience and Remote Sensing*, 50(1): 180-192. <https://doi.org/10.1109/TGRS.2011.2161637>